Carbon 126 (2018) 532–543

Contents lists available at ScienceDirect

Carbon

journal homepage: www.elsevier.com/locate/carbon

Sub-μm *c*-axis structural domain size of graphene paper uncovered by low-momentum phonon scattering

Meng Han [a, 1], Jing Liu [a, 1], Yangsu Xie [b, a], Xinwei Wang [a, *]

[a] 2010 Black Engineering Building, Department of Mechanical Engineering, Iowa State University, Ames, IA 50011 United States
[b] College of Chemistry and Environmental Engineering, Shenzhen University, Shenzhen 518055, Guangdong, PR China

ARTICLE INFO

Article history:
Received 5 September 2017
Received in revised form
13 October 2017
Accepted 20 October 2017
Available online 1 November 2017

ABSTRACT

The *c*-axis thermal conductivity (k_c) of graphene paper (GP) is measured from 295 K to 12.3 K and extrapolation is used to identify the residual thermal reffusivity at the 0 K limit. To uncover the structural domain size based on the residual thermal reffusivity, we develop an anisotropic specific heat model to identify the phonons that sustain the heat conduction along the *c*-axis. This model predicts a *c*-mean free path (MFP) of 165 nm for graphite at room temperature (RT), very close to the value of 146 nm by molecular dynamics (MD) modeling. For widely studied normal graphite materials, this model predicts a structure domain size of 375 nm, close to the 404 nm grain size uncovered by transmission electron microscopy. Using our model, the *c*-MFP induced by defect in the GP is evaluated at 234 nm based on the low-momentum phonon scattering. This structural domain size significantly exceeds the graphene flake thickness (1.68–2.01 nm) in our GP, uncovering excellent *c*-direction atomic structure order. By subtracting the residual thermal reffusivity, the defect-free k_c and *c*-MFP of GP are obtained. At RT, the defect-free k_c is 9.67 $Wm^{-1}K^{-1}$, close to 11.6 $Wm^{-1}K^{-1}$ of graphite from the recent MD simulations.

1. Introduction

Since its first discovery in 2004 [1], graphene has been extensively studied due to its intriguing properties such as extremely high electrical [2] and thermal conductivity [3], large specific surface area [4], and high mechanical strength [5]. In recent years, graphene and graphene-based materials have seen promising applications in devices like photodetectors [6], solar cells [7], flexible touch screen [8], sea water desalination [9], gas purification and liquid separation [10] and thermal interface materials [11], etc. Understanding the mechanisms underlying these remarkable properties help broaden the applications of graphene.

In the last decades, different approaches have been used to characterize the thermal transport properties of graphene which are of great importance in its applications. The first experimental approach was made through development of the optothermal Raman measurement technique [3,12–14]. The extracted thermal conductivity varies in a large range and can be as high as 5000 $Wm^{-1}K^{-1}$ at room temperature (RT) [3]. This value exceeds that of bulk graphite in the in-plane (*a*-axis) direction (~2000 $Wm^{-1}K^{-1}$ at RT) [15]. Following experimental work reported values ranging from hundreds to thousands of $Wm^{-1}K^{-1}$ [16–18]. The large discrepancy among these experimental results is attributed to many factors including the sample lateral size, the defect level, the grain size and orientation and the strain distributions, etc.

Compared with the extensive investigations of the *a*-axis thermal conductivity (k_a), thermal transport along the *c*-axis of multilayered graphene is lack of attention. Most work along the *c*-axis is mainly focused on the interface thermal resistance between graphene films and other materials like metals [19,20] and dielectrics [21]. Direct characterization of the *c*-axis thermal conductivity (k_c) of graphite can be dated back to several decades [22,23], leaving the underlying mechanism for the two to three orders of magnitude lower values (5.7–6.8 $Wm^{-1}K^{-1}$) not clearly uncovered [23,24]. Early work employed a classic kinetic theory to describe the thermal transport along the *c*-axis [25]. The estimated *c*-axis phonon mean free path (*c*-MFP) is just a few nanometers, seemingly consistent with the small *c*-axis thermal conductivity. However, several recent theoretical calculations and experimental measurements suggested that the *c*-MFP can be much longer. Wei et al. [26] performed molecular dynamics (MD)

* Corresponding author.
E-mail address: xwang3@iastate.edu (X. Wang).
[1] Equal contribution authors.

https://doi.org/10.1016/j.carbon.2017.10.070
0008-6223/

simulations on graphite thin films and found that k_c does not converge even when the film thickness is increased to 15 nm. Harb et al. [27] performed time resolved x-ray diffraction (XRD) on a graphite thin film with a thickness of 35 nm and reported a value of only 0.7 $Wm^{-1}K^{-1}$, much lower than the well-accepted value of bulk graphite. These relatively lower values indicate that the actual *c*-MFP of bulk graphite are longer than 15 nm and 35 nm. Later work by Sadeghia et al. [28] estimated an average *c*-MFP of 20 nm at 300 K with a theoretical calculation based on the full phonon dispersions. Recent MD simulations of Wei et al. [29] observed the contribution of phonons to the *c*-axis with a long *c*-MFP in the order of hundred nanometers. Most recent experimental work by Fu et al. [30] measured k_c of graphite films with different thicknesses by employing the 3ω method and gave strong evidence that the average *c*-MFP at RT can be more than 100 nm. Similar work by Zhang et al. [31] conducted the time-domain thermoreflectance (TDTR) measurements on graphite films within a larger range of sample thicknesses and ambient temperatures. They found that the *c*-MFP is in the order of 100–200 nm at RT. With these progressive work, it starts to be accepted that the *c*-MFP of graphite is comparable to or not much smaller than that in the *a*-axis direction.

Despite the tremendous academic research, direct applications of graphene and thin graphite films in industry are still limited, mainly due to the difficulties in producing large area graphene with high quality. In recent years, graphene based materials like 3-D graphene foam (GF) and freestanding graphene paper (GP) have seen promising applications in the industry [32–35]. GP is a bulk material composed of graphene flakes and shows large anisotropic properties like graphite. Although the graphene flakes in GP are relatively small, GP has a reported large thermal conductivity (~1000 $Wm^{-1}K^{-1}$ at RT) [36] and electrical conductivity (~1.57×10^5 Sm^{-1}) [37], much larger than those of other graphene-based materials. GP can be fabricated through different methods including chemical reduction [38], acid intercalation followed by thermal exfoliation [39] and heating graphene oxide paper in different environments, among which the heating and annealing process is of great efficiency [40]. To better understand the thermal transport properties and the inner structure of GP and provide more information for the applications of GP in thermal materials, our recent work performed experimental measurements on the highly reduced and ordered GP from RT down to very low temperatures [41]. The GP sample shows high in-plane thermal conductivity (~600 $Wm^{-1}K^{-1}$) at RT and an interesting switch-on phenomenon when the temperature goes down to about 245 K.

In this work, we report on measurement of the cross-plane (*c*-axis) thermal conductivity and thermal diffusivity (α_c) of the same GP by using a pulsed laser-assisted thermal relaxation 2 (PLTR2) technique [42]. A phonon transport model is proposed to split the phonons propagating in different directions and account the contribution of only low-frequency phonons to the heat capacity and thermal transport along the *c*-axis. This model takes into account the large anisotropies of phonon dispersions and phonon group velocities in GP and quantitatively explains the very small k_c yet very long *c*-MFP. Then the thermal reffusivity (Θ) theory is used to study the *c*-MFP and defect level in GP and give an estimation of the *c*-axis crystallite size. The thermal reffusivity (reciprocal of thermal diffusivity) is defined in our lab to characterize the normalized thermal resistivity induced by the energy carriers like electrons and phonons. The advantage of thermal reffusivity is that it solely depends on the propagation of energy carriers and can provide sound estimation of the structural domain size and defect level embedded in the materials. After subtracting the defect effect, the defect-free k_c of GP is evaluated to the first-order estimation.

2. Experimental details

The laser flash technique is widely used for the measurement of thermal diffusivity [43–45]. In this method, a short laser pulse is used to uniformly irradiate the front surface of the specimen and induces a local temperature rise. Then heat transfer occurs from the front surface to the rear surface across the specimen. The temperature response of the rear surface is detected by an infrared detector or thermal couples and used to extract the thermal diffusivity of the specimen. However, in some cases, such as very thin/small sample and under very low temperatures, the thermal couples and infrared detector are difficult to collect the thermal response signals. Thus, in the present work, the PLTR2 technique is used to characterize the thermal transport properties of GP in the cross-plane direction. The PLTR2 technique, which is an improvement on the PLTR technique in our group [46], is capable of determining thermal transport properties of films both in the in-plane and cross-plane directions [42,47].

2.1. Sample preparation and characterization

In the PLTR2 technique, the heating process is the same as in the typical laser flash method. Instead of using an infrared detector or thermal couples, the temperature response is detected by variations of the electrical resistance of an Iridium (Ir) coating on the rear surface of the sample. The GP is purchased from Graphene Supermarket. Note that GP has very high electrical conductivity, so that it should be isolated from the Ir coating to make sure only the electrical resistance variation induced by the rear surface temperature evolution is detected. In the present work, we use a polyethylene terephthalate (PET) film as an isolator to separate Ir coating from GP.

Fig. 1 shows the schematic of the sample preparation process in this work. A 500 nm-thick PET film is purchased from Goodfellow. A 20 nm Ir is sputtering coated on one side of the PET film within an area similar to that of the GP sample (13.5×1.9 mm^2). A small drop of PMMA/toluene solution (1% mass percentage) is put on one side of the GP sample for the adhesion of GP and PET. The PMMA/toluene solution is prepared by dissolving PMMA particles in toluene solvent. The PMMA particles are purchased from Sigma-Alorich. 0.2 g PMMA particles are mixed with 19.8 g toluene solvent in a closed glass bottle and then stirred with a magnetic stirrer for more than 24 h at 50 °C to make sure that the PMMA particles are totally dissolved in toluene. Immediately after the solution expands and covers the whole side, the GP sample is attached to the PET film with the solution facing the uncoated side of PET film. In a few hours, the toluene solvent will volatilize and good attachment among GP, PMMA and PET forms. Then the sample is suspended between two electrodes with the Ir coating facing the electrodes and forming an electrical circuit. (The electrodes are made from Silicon wafers and coated with 180 nm Ir to provide high electrical and thermal conductance.) In this step, silver paste is used to optimize the electrical and thermal contacts between the Ir coating and the electrodes. The most challenging thing is to make sure that only the Ir coating not the GP is in the electrical circuit with such thin PET and PMMA film.

In the PLTR2 model, the thicknesses of the film layers are key parameters during the thermal relaxation process. However, in the micro/nanometer scale, the thickness is difficult to determine directly, especially for the PMMA film that forms from solution. To get a better evaluation of the thicknesses of the films, the thermalgravimetric analysis (TGA) is performed on the sample after the PLTR2 measurements. With the lateral dimensions measured under an optical microscope and the densities referred from literature, the thicknesses of GP, PMMA and PET layers are determined,

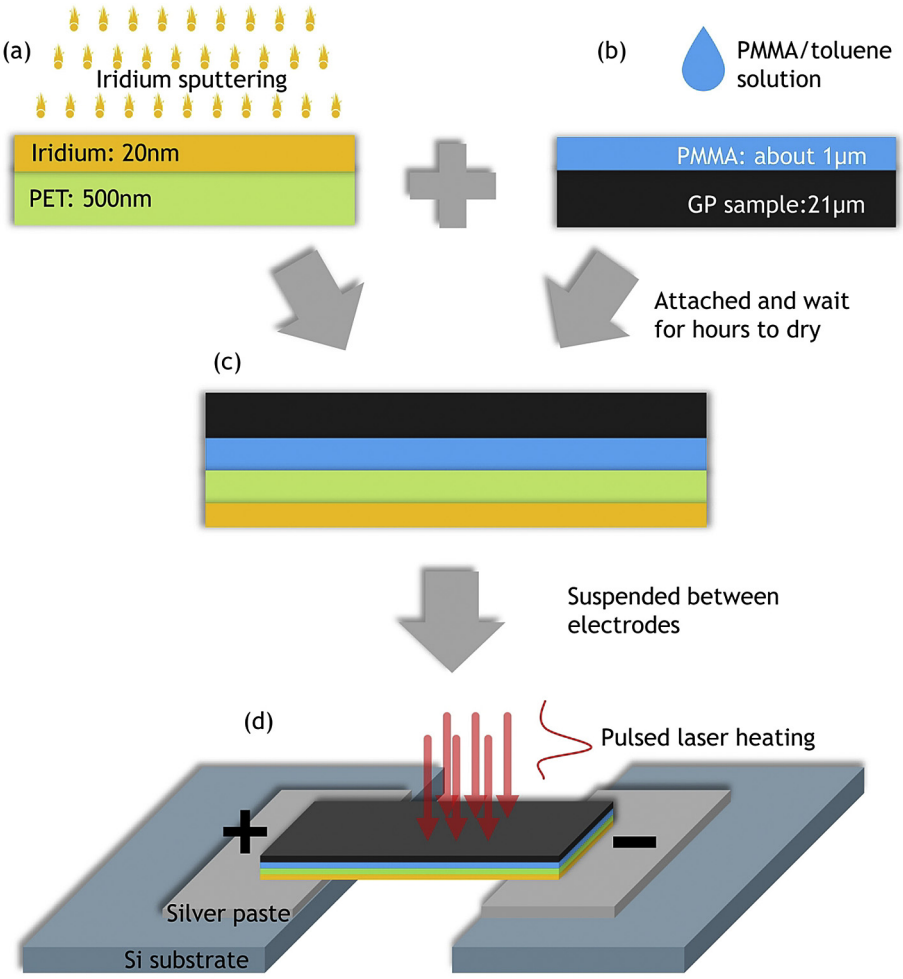

Fig. 1. Sample preparation process. (a) Sputtering coating of 20 nm Ir on one side of the PET film; (b) A small drop of PMMA/toluene solution is put on one side of GP and expands to cover the whole side; (c) The GP sample is attached to the PET film immediately after the expansion of the solution with the solution facing the uncoated side of PET film; (d) The multilayered sample is suspended between two electrodes with the Ir coating facing these electrodes. Then the sample is connected to an electrical circuit through the Ir coating and exposed to the pulse laser heating for the PLTR2 measurements. (A colour version of this figure can be viewed online.)

respectively. In the present work, the lateral dimensions for the TGA sample is 3.7 × 1.9 mm^2 and the densities of GP, PMMA and PET used here are 2210, 1180 and 1350 kgm^{-3}, respectively. Fig. 2a shows the TGA results of the sample, from which we can see two clear peaks in the first order differential curve (red) of the mass loss percentage. These two peaks represent the mass loss from the evaporation of the PMMA and PET films. From the peak areas, the total mass of the PMMA and PET films in the sample is calculated at 15.4 μg. The thickness of PET is determined as 0.58 μm by measuring the mass of a single PET film with a lateral dimension of 4.87 × 3.80 cm^2. This value is consistent with the product description of 0.5 μm within 20% uncertainty. Thus, the thickness of the PMMA film is determined as 1.2 μm. In argon atmosphere, GP and Ir will stay unchanged at temperatures up to 600 °C. The rest of the material after the TGA contains only GP and Ir and the mass can be easily determined. The 20-nm thickness of the Ir coating can be well controlled in our sputtering system and the mass takes no more than 1% of the rest material after the TGA. Assuming homogeneous thicknesses of these films in the sample, the thicknesses of the GP, PMMA and PET are 21.4, 1.2 and 0.58 μm respectively. These values will be used in the numerical calculations for data processing which will be detailed in the following section.

The structure of the GP material is characterized by using XRD, Raman spectroscopy and scanning electron microscope (SEM). Fig. 2b shows the XRD spectrum of the GP, from which a sharp peak can be seen at 26.6° of 2θ. This peak corresponds to the (002) plane of GP, from which the interlayer spacing of GP is determined at 3.35 Å, the same as that of pristine graphite [48]. This also proves that the GP here has high quality and excellent ordered structure. The crystallite size cannot be determined from XRD as the peak linewidth reaches the limit of machine broadening. Fig. 2c shows the Raman spectra from different positions of the GP sample. Two clear peaks can be seen at about 1581 and 2719 cm^{-1}, which correspond to the G peak and 2D peak, respectively. The D peaks in all spectra are invisible, indicating rare defects and high crystallinity of the graphene flakes. In addition, all the spectra are almost consistent with each other, meaning the numbers of layers in the graphene flakes have high consistency. The ratio of the integrated intensities of G peak to 2D peak is estimated at 0.7, corresponding to 5–6 layers graphene in the flakes [49]. Fig. 2d shows the SEM image of GP under a 500 × magnification, from which we can see the smooth surface and clear stacking layered structure of the graphene flakes. The x-ray photoelectron spectrometer (XPS) study has also been conducted on the GP in our previous work [41]. The result shows that the elemental composition is C 1s (98.91%), O 1s (0.66%) and F 1s (0.43%), indicating that the GP is of highly pure

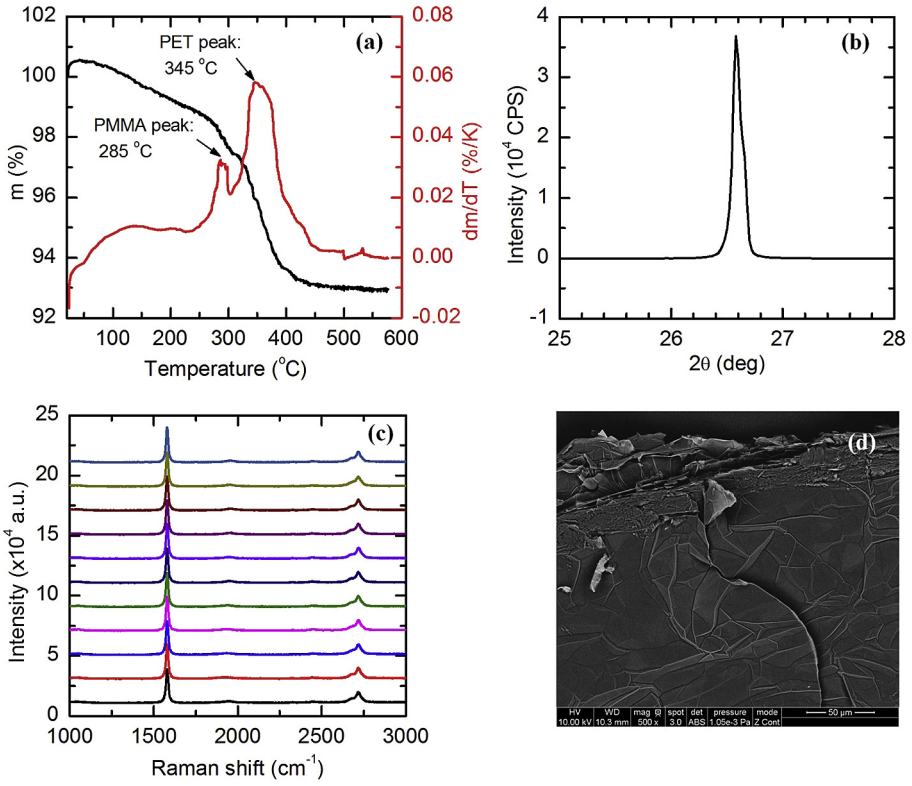

Fig. 2. Sample characterization. (a) TGA results of the multilayered sample with the black curve as the variation of mass percentage and red curve as the first deviation of the variation of mass percentage. The two peaks in the red curve represent the mass loss from evaporation of PMMA and PET, respectively. (b) XRD spectrum of the GP sample, which shows a clear single peak at 26.6° of 2θ. (c) Raman spectra from different positions of the GP sample from which the layer number in graphene flakes is determined. (d) SEM image of the GP sample, showing smooth surface and clear stacking structure. (A colour version of this figure can be viewed online.)

carbon material.

2.2. Experimental setup and physical model for thermal characterization

The thermal conductivity of GP in the cross-plane direction is measured by using the PLTR2 technique. Fig. 3 shows the schematic of the experimental setup. During the measurement, the sample is kept in a vacuum chamber with a pressure less than 1×10^{-3} torr to eliminate the influence of heat convection from the sample surface. The environmental temperature is controlled by the cooling head under the sample and substrate. A constant DC current is fed to the sample and forms an electrical circuit through the back-side Ir coating. The electrical resistance and voltage variations of the Ir coating are detected by an oscilloscope (Tektronix MDO 3052 Mixed Domain Oscilloscope). A nanosecond pulsed laser is used to irradiate the front surface of the GP and heat transfer occurs in the GP/PMMA/PET multilayer films. The temperature of the Ir coating will evolve to a maximum value and then decrease slowly as the heat dissipates to the environment. In our measured temperature range, the electrical resistance of Ir is linearly proportional to the temperature variation. Thus, the temperature response can be detected by the electrical resistance or voltage changes of the Ir coating.

In this work, the laser pulse width is about 8 ns (shown in Fig. 3) which is more than three orders of magnitude smaller than the cross-plane thermal relaxation time (at the μs scale). In this case, the finite pulse duration effect is negligible. We use a Si photodiode connected with the oscilloscope to trigger the sample voltage measurement after laser pulse. The position of the laser pulse in the time scale is taken as the beginning time of the thermal relaxation which is of key importance in the laser flash model. With a cover (not shown in Fig. 3) before the sample we can make sure that only the suspended part of the sample is irradiated. Due to the much larger original laser spot size (diameter of about 3.5 cm) compared with the sample length (about 7 mm as suspended and irradiated), it is true that the pulse energy is uniformly absorbed by the irradiated sample within a small depth at the front surface. In practice, heat will dissipate in the in-plane and cross-plane direction simultaneously. While in this work, with a large ratio of characteristic lengths in the two directions (mm scale to μm scale), we can safely simplify the thermal transport as one-dimensional (1D) in the cross-plane direction and then in the in-plane direction. Our recent work [41] shows that the thermal diffusivity in the in-plane direction of the GP sample is no larger than 5.57×10^{-4} m^2s^{-1} before switch-on. The characteristic thermal relaxation time is defined as $t_c = L^2/\alpha$. With the in-plane characteristic length taken as 7 mm, the in-plane t_c is calculated as 88 ms.

For comparison, the thermal relaxation time in the cross-plane direction (t_{cr}) is no longer than 100 μs (Fig. 4a), nearly three orders of magnitude smaller than that in the in-plane direction. This means during the time of thermal transport in the cross-plane direction, thermal transport in the in-plane direction is negligible. When the temperature reaches uniform distribution in the cross-plane direction, heat dissipation starts in the in-plane direction to the electrodes. This simplification in the PLTR2 technique has been proved in determining thermal diffusivity of thin films both in the cross-plane and in-plane directions from a single measurement [42,47].

For multilayered films, with the 1D heat transfer model, the

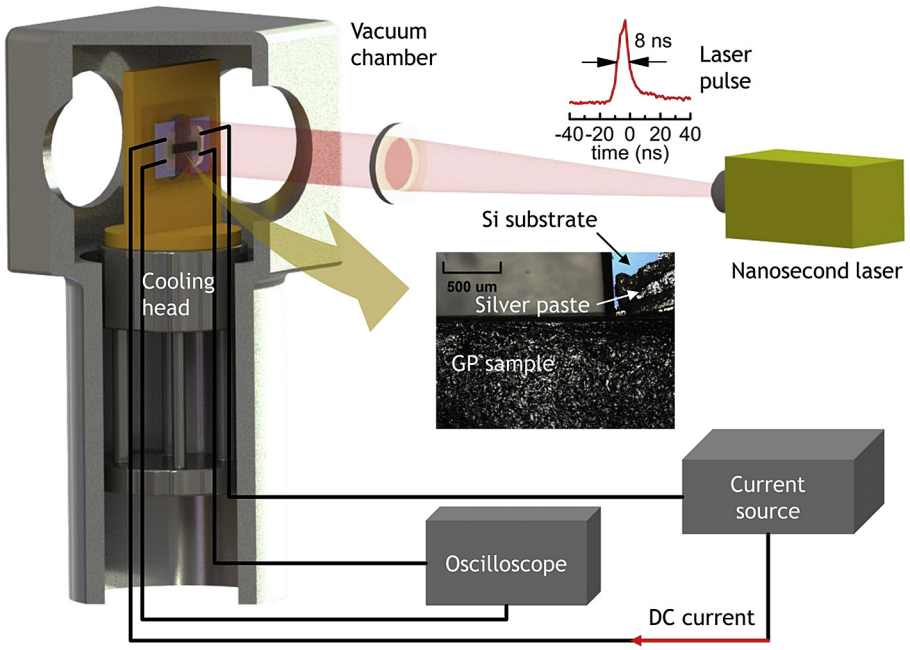

Fig. 3. Schematic of the experimental setup of the PLTR2 technique. The sample is put into a vacuum chamber and the environmental temperature is controlled by the cooling head under the substrate. The Ir coating at the rear surface is connected to a current source and an oscilloscope for detecting of the rear surface temperature. A nanosecond pulsed laser irradiates the front surface of the sample to introduce temperature gradient and heat conduction across the sample. The insets show the laser pulse duration and part of the GP/PMMA/PET multilayered sample prepared in this work. (A colour version of this figure can be viewed online.)

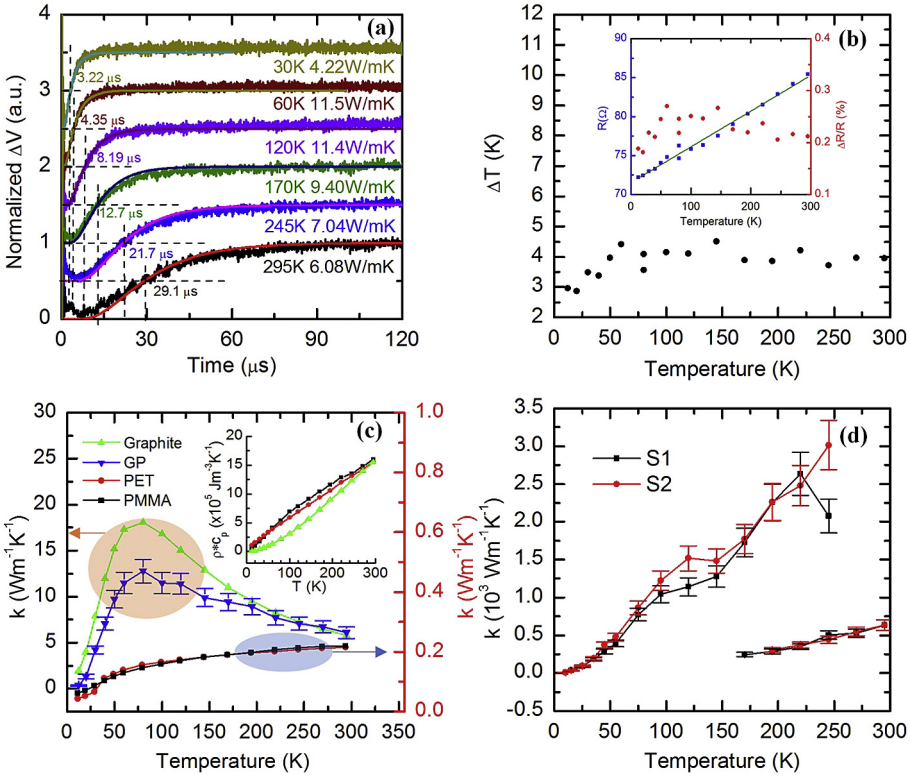

Fig. 4. PLTR2 measurement results. (a) Normalized rising curves and the half rise times at several of our environmental temperatures. Also shown are the best fitting curves from the numerical calculations and the fitted k_c at these temperatures. (b) The maximum temperature rises at the rear surface after the laser pulse irradiation. The inset shows the initial electrical resistances and the maximum relative electrical resistance rises of the Ir coating against temperature. (c) The fitted k_c of GP against temperature. Also shown are the thermal conductivities of PMMA, PET and Graphite from literature [55–57]. The inset shows the volumetric heat capacity of PMMA, PET and graphite used in the fitting process [52–54]. (d) In-plane thermal conductivity of GP characterized in our recent work [41]. (A colour version of this figure can be viewed online.)

transient temperature rise $T(x,t)$ can be obtained by solving the governing equation for each layer:

$$\frac{\partial T_i(x,t)}{\partial t} = \alpha_i \frac{\partial^2 T_i(x,t)}{\partial x^2}, \quad i = 1,\ 2,\ 3 \tag{1}$$

with the initial value $T_1(x,0) = Q/A\tau_{opt}\rho_1 c_{p,1}$, for $0 < x < \tau_{opt}$, $T_1(x,0) = 0$, for $x > \tau_{opt}$ and $T_{2,3}(x,0) = 0$. Here, $i = 1, 2, 3$ represent the GP, PMMA and PET layers, respectively. Q is the absorbed pulse energy; A is the irradiated surface area of the sample; $\rho_1 c_{p,1}$ is the volumetric heat capacity of the irradiated layer; τ_{opt} is the optical absorption depth of the irradiated layer and is taken as 31.7 nm for GP [50].

Analytical solutions to two-layered or three-layered composites have been described in detail [45,51]. However, those solutions are always complicated. In the present work, instead of solving the governing equation analytically, a numerical method is used to simulate the 1D thermal transport across the GP/PMMA/PET three-layered film and obtain the temperature response at the rear surface. In the simulation process, each layer film is assumed to be homogenous with the densities, specific heat (inset in Fig. 4c) and thicknesses are all known parameters [52–54]. Thermal conductivities of the PMMA and PET layer are also taken from literature (Fig. 4c) [55–57]. The only unknown parameter is k_c of GP. With different trial values of k_c input in the simulation process, different temperature response curves at the rear surface can be obtained. Then the least square method is used to extract the value that can give the best fit of the experimental one.

3. Thermal conductivity variations against temperature

In the PLTR2 measurements, the GP sample is 7×1.9 mm^2 with a thickness of 21.4 μm. The initial electrical resistance of the Ir coating is 85.4 Ω. We feed a DC current of 11.6 mA at RT through the sample and measure its voltage to track the temperature evolution. The initial electrical resistance changes with the environmental temperature and we choose different feeding current at different temperatures to make sure the overall initial voltage does not change too much. The nanosecond laser irradiates the sample with an original laser spot size of about 3.5 cm and a frequency of 1 Hz. The pulse energy is also chosen at different environmental temperatures to give sufficient signal to noise ratio yet small temperature rises. Fig. 4a shows the experimental data from the PLTR2 measurements and the best simulation curves under several environmental temperatures in this work. We can see the simulation curves and the experimental data match with each other very well, despite the small discrepancies at the beginning time. The discrepancies come from the electrical disturbance from the laser system when the pulse is feeding which will disappear soon and have negligible influence on the overall fitting results. The extracted k_c of GP under these temperatures are also noted in Fig. 4a. Also shown in Fig. 4a are the half rise times which decrease rapidly from 29.1 μs to 3.22 μs as the environmental temperatures decrease from 295 K to 30 K. This means the measurement is able to detect thermal relaxation time down to several microseconds scale which in other words proves the ability of quick response of the PLTR2 technique. The inset of Fig. 4b shows the initial electrical resistances of the Ir coating before the laser pulses against the environmental temperatures. From linear fitting, the temperature coefficient of electrical resistance of Ir coating is determined. The red circles in the inset of Fig. 4b are the relative maximum electrical resistance rises after the laser pulse heating. With the determined electrical resistance temperature coefficient and the maximum electrical resistance rises, the maximum temperature rises are calculated. Fig. 4b shows the maximum temperature rises at the rear surface of the sample after the laser pulse. All these maximum temperature rises are smaller than 5 K (mainly around 4 K). At very low temperatures, the maximum temperature rises are only around 3 K. In this case, the thermal property changes of GP during the measurement under a single environmental temperature should be negligible.

Fig. 4c shows the determined k_c of GP (blue triangles) from RT (295 K) down to very low temperature (12.3 K). The error bars show the measurement uncertainty in this work. It has been demonstrated that when the trial values change by ±10%, the simulation curves obviously deviate from the experimental data. Note that, at each environmental temperature, we take the measurements more than 100 times and get the average data. This also highly suppresses the high-frequency noises in the oscilloscope and reduce the uncertainties of our measurement results. The inset in Fig. 4c shows volumetric heat capacities ($\rho \cdot c_p$) of PMMA, PET and graphite used in the calculation of simulation curves from literature [52–54]. Here, c_p of GP is taken from that of graphite, which should have no significant difference with the high purity GP studied here. The red circles and black rectangles in Fig. 4c are the thermal conductivities of PET and PMMA [55–57]. For comparison, k_c of a well-annealed pyrolytic graphite with well-oriented crystalline layer structure from literature is also shown in Fig. 4c (green rectangles) [58]. At RT, k_c of GP is determined as 6.08 ± 0.6 Wm^{-1}K^{-1}, consistent with the well-accepted value of 5.7–6.8 Wm^{-1}K^{-1} of graphite [23,24]. In the range of 295 K–200 K, k_c of GP and graphite are close and when temperature goes below 200 K, k_c of GP is getting smaller than that of graphite. At 80 K, k_c of GP and graphite will reach their peak values and will decrease rapidly as temperature goes much lower. This k_c variation against temperature can be explained by the behavior of defect-phonon scattering and will be detailed latter.

It is well known that electrons have negligible contribution to the thermal transport in graphene or graphite and the thermal transport ability is governed by the occupied phonon modes and phonon scattering. At relatively high temperatures (higher than 180.5 K, the effective c-axis Debye temperature corresponding to the cut-off frequency at 4 THz [59]), the density of occupied phonon modes is almost constant. The thermal conductivity is limited by the phonon scattering including Umklapp phonon-phonon scattering (U-scattering), phonon-boundary scattering and phonon-defect scattering. As temperature goes down, lattice vibrations get weaker, the U-scattering is correspondingly less activated but still dominates, which leads to the increase of k_c. When temperature is getting lower from 180.5 K, the occupied phonons modes start reducing but slightly, the U-scattering keeps getting weaker, the phonon-boundary and phonon-defect scattering start to dominate. That is why k_c of GP and graphite keeps increasing from about 295 K to 80 K, but start to deviate from each other at about 200 K due to their different domain sizes and defect levels. As temperature goes down from 80 K and approaches 0 K, k_c decreases dramatically due to the large decreasing of phonon occupation at extremely low temperatures. The behavior of the phonon transport of GP and graphite along the c-axis will be detailed in the following section.

Fig. 4d shows the measured k_a of GP against temperature in our recent work [41]. From Fig. 4c and d we can see when the temperature is not too low, k_a is more than two orders of magnitude larger than k_c, which is consistent with the large anisotropy of pristine graphite. When temperature is getting lower from 80 K to 0 K, both k_a and k_c continue decreasing and follow similar trend with that of the specific heat [60]. This indicates that in this temperature range the dominating scattering mechanisms are the boundary and defect scattering but the thermal transport ability is

mainly controlled by the density of phonon modes occupation.

To confirm the accuracy of the PLTR2 measurements, k_c of the same GP at RT is measured by using the Photothermal (PT) technique [61,62]. Fig. 5a shows the schematic of the PT principle. A continuous laser is modulated with different frequencies in a large frequency range by a function generator. The modulated laser is then directed to and focused on the GP sample. The sample is heated and thermal radiation variation occurs at the front surface of the sample. This thermal radiation is strongly affected by the thermal transport properties of the sample and is detected by an infrared detector. The thermal radiation signals are then pre-amplified and directed to a lock-in amplifier (not shown in Fig. 5a). The phase shifts between the thermal radiation and the incident laser beam are extracted. By fitting the experimental phase shifts using the theoretical ones (which are calculated based on the thermal transport properties of the sample) over the modulation laser frequencies, we can extract the unknown properties of the sample (here is k_c of GP). In this work, the modulation laser frequency ranges from 200 Hz to 4000 Hz. The lateral dimension of the sample for the PT measurement is about 1×1 mm^2, much smaller than the laser spot size (about 4×8 mm^2). Thus, we can safely assume that the front surface of the sample is uniformly heated and thermal transport in the sample is 1D in the cross-plane direction. Details of the PT technique and the 1D heat transfer model can be found in our previous work [62,63].

The fitting process is conducted by using a well-developed program in our lab. The thickness of the sample here is measured at 21.9 μm, consistent with that of the sample in the PLTR2 measurements, considering the thickness measurement uncertainty. The density and heat capacity are taken from that of graphite like in the PLTR2 measurements. With these physical properties fixed, different trial values of k_c are used to calculate the theoretical phase shifts over the modulation frequency range. The value that gives the least square deviation between the theoretical phase shifts and the experimental ones is taken as the real k_c of GP. Fig. 5b shows the fitting results, from which we can see the best fitting curve (red curve) and the experimental data (black circles) match well with each other. Also shown in Fig. 5b are the calculated theoretical curves when k_c changes by 10% (the green and blue ones). We can see these two curves deviate clearly from the best fitting one and the experimental data. Therefore, we can conclude that, k_c of GP is 5.38 ± 0.54 Wm^{-1}K^{-1} at RT, with an uncertainty of 10%. This value is close to 6.08 ± 0.6 Wm^{-1}K^{-1} determined by the PLTR2 technique. This PT measurement on GP at RT helps verify the accuracy of the PLTR2 measurements. Note that the PT technique cannot be used for cryogenic measurement since at very low temperatures, the thermal radiation from the sample surface has a very long wavelength (sub-mm) while our thermal radiation detector only detects radiations at a few μm wavelength. So the PLTR2 technique is adopted for cryogenic measurement.

4. Thermal reffusivity and structure domain size

4.1. Low-frequency phonons-dominated thermal transport along the c-axis

It is well accepted that thermal transport in graphene and graphene based materials is dominated by phonons [64,65]. This also holds true in GP. As studied by the XRD, XPS, SEM and Raman techniques, the GP sample here is composed of highly purified and highly ordered graphene flakes. Fig. 6a shows the schematic of the cross-section view of the GP sample, from which we can see the graphene flakes is highly ordered. Also from the XRD technique, the interlayer spacing of GP is determined at 3.35 Å, the same as that of pristine graphite as shown in Fig. 6b. Thus, in this section, thermal transport in GP is studied with reference to phonon transport in graphite.

Phonon dispersion of monolayer graphene has been studied extensively [66–70], which can give the most information about phonon transport in graphene. For monolayer graphene, as there is only one layer of carbon atoms connected with strong sp^2 bonds, thermal transport is two-dimensional (2D) from contribution of the whole phonon branches. While for graphite, the phonon dispersion is kind of different [71–74], considering the weak Van der Waals force among layers. Fig. 7a shows the reproduced phonon dispersion from Nichlow's work [71], both in the Γ-A and Γ-M directions. The phonon modes are doubly degenerate at relatively high frequencies due to weak coupling among layers. The 'prime' (LO′ or ZO′) indicates that the two equivalent atoms in a layer vibrate in phase, but with a phase difference of 180° with respect to the two atoms in the neighboring layer [72]. Compared with phonon dispersion in monolayer graphene, the 2D thermal transport in graphite is only valid till some low-bound cut-off frequency. Below this frequency, strong energy coupling with the cross-plane phonon modes appears and heat starts to propagate in all directions, which reduces the contribution from these low-frequency phonon modes to heat transport along basal planes to negligible values [75].

From the phonon dispersion in Fig. 7a, there is a physically reasonable reference frequency for the on-set of cross-plane coupling (4 THz), which is the ZO' phonon branches at the Γ point. Fig. 7a also shows that most of the phonon branches in the (001) plane are all long-wavelength phonons with frequencies under 4 THz. There are also optical phonon branches at about

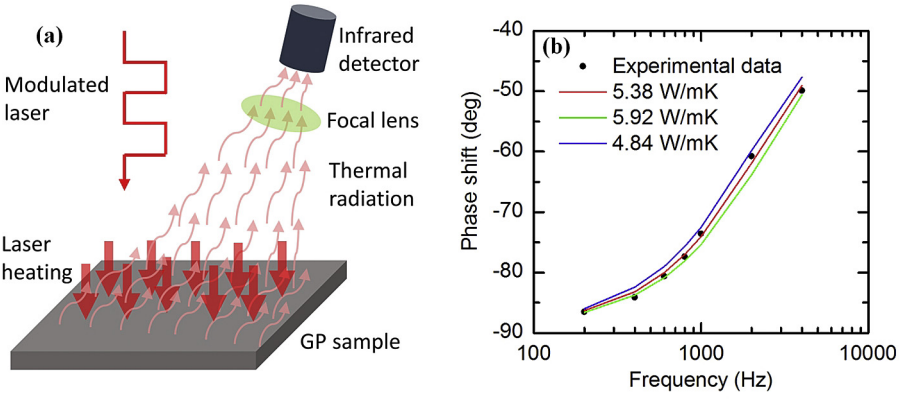

Fig. 5. k_c measurement by the PT technique: (a) schematic of the PT technique (b) phase shifts fitting to extract k_c of GP at RT. (A colour version of this figure can be viewed online.)

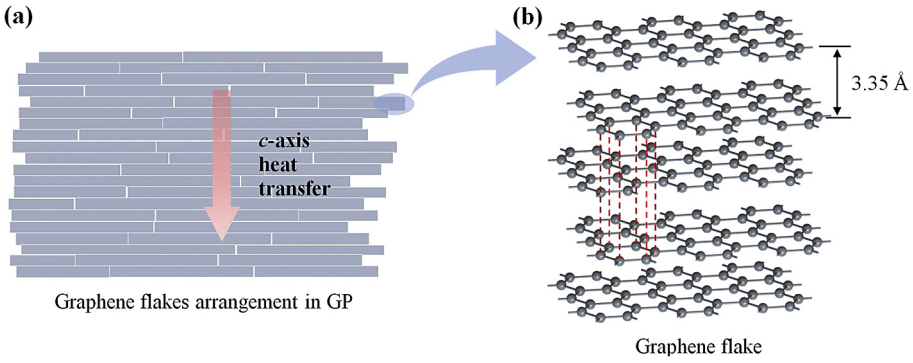

Fig. 6. Schematic of our GP sample (not to scale). (a) Graphene flakes arrangement in the GP sample. (b) AB stacking of graphene sheets in the graphene flakes. (A colour version of this figure can be viewed online.)

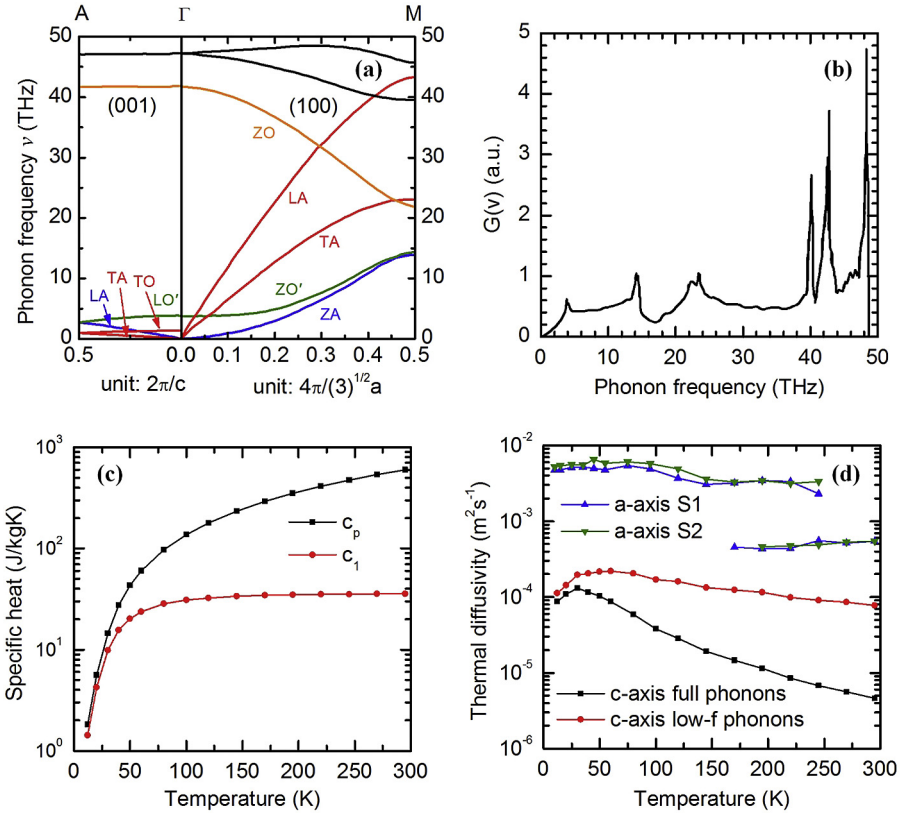

Fig. 7. Calculation from phonon dispersions. (a) Phonon dispersions of graphite in the (001) and (100) directions [71]. (b) Density of state of phonons of graphite [71]. (c) Specific heat (c_1) calculated from only low-frequency phonons that sustain c-axis heat conduction and specific heat (c_p) calculated from the whole phonon branches. (d) Cross-plane and in-plane thermal diffusivities of GP against temperature calculated in this work and in our previous work, respectively [41]. (A colour version of this figure can be viewed online.)

41 THz and 47 THz. However, these high-frequency phonons have small phonon group velocities with very narrow frequency ranges. Besides, phonons obey the Bosons-Einstein distribution as $\langle n\rangle = 1/[\exp(h\nu/k_BT) - 1]$, where $\langle n\rangle$ is the particle numbers in the quantum state, h the Planck's constant, k_B the Boltzmann constant and ν the phonon frequency. From this equation we can see that the phonon numbers are much smaller at high phonon frequencies. For example, at 41 and 47 THz, $\langle n\rangle$ correspond to values of 1.27×10^{-3} and 4.78×10^{-4}, respectively, about three orders of magnitude smaller than 1.09 at 4 THz. In this case, the contribution of these high frequency phonons to thermal transport can be negligible. Thus, we can approximately claim that the thermal transport along the c-axis is only from contribution of low-frequency phonons under 4 THz.

The phonon thermal conductivity (k_p) can be written as [75]:

$$k_p = \sum_j \int C_j(\omega) v_j^2(\omega) \tau_j(\omega) d\omega, \tag{2}$$

where $\omega = 2\pi\nu$ is the phonon frequency; C_j the contribution to heat capacity from the jth branch; $v_j = d\omega_j/dq$ the phonon group velocity of the jth branch; τ_j the phonon relaxation time. The summation is performed over phonon branches j, which includes one longitudinal acoustic (LA) and two transverse acoustic (TA) branches.

From the (001) plane in Fig. 7a the phonon group velocities v_{LA} and v_{TA} are calculated at 1960 m/s and 700 m/s, respectively. The average phonon group velocity (v) can be calculated as $3/v = 1/v_{LA} + 2/v_{TA}$ [76]. Thus, we have v = 890 m/s along the c-axis. The phonon mean free path (l) is related to the relaxation time as $l = v\tau$. As mentioned before, the phonon relaxation time is from various scattering mechanisms including U-scattering, phonon-boundary scattering and phonon-defect scattering. According to the Matthiessen's rule, the limitation of thermal transport from these scattering mechanisms are additive, which can be expressed as the following equation:

$$\frac{1}{\tau} = \frac{1}{\tau_U} + \frac{1}{\tau_{boundary}} + \frac{1}{\tau_{defects}}, \quad or \quad \frac{1}{l} = \frac{1}{l_U} + \frac{1}{l_{boundary}} + \frac{1}{l_{defects}}. \tag{3}$$

As temperature decreases, U-scattering weakens which leads to the increase of τ_U. As temperature approaches 0 K, the $1/\tau_U$ or $1/l_U$ term vanishes, leaving only the boundary and defect scattering terms.

Phonons are quantized particles representing lattice vibrations. Lattice vibrations are directly related to atomic interactions. Strictly speaking, the cross-plane atomic interactions directly lead to c-axis heat conduction. This heat conduction will directly exchange energies of the phonons involving cross-plane atomic interactions. Here we introduce the anisotropic phonon heat capacity concept: C_1 and C_2. C_1 is the volumetric heat capacity of phonons involving cross-plane atomic interactions and is termed c-axis heat capacity, although it is a scalar. C_2 is the volumetric heat capacity of phonons involving in-plane atomic interactions, which should be close to that of monolayer graphene. Under this theory, in our experiment the thermal transport along the c-axis can be interpreted as a two-step process. As the cross-plane only supports energy coupling among low frequency phonons, energy absorbed by the large part of high-frequency phonons in the upper layers should first be transferred to the low-frequency phonons through in-plane atomic interactions in the same layer and then to the down layers through cross-plane atomic interactions.

This two-step process can be described by the following equations:

$$\frac{\partial C_1 T_1}{\partial t} = k_c \cdot \frac{\partial^2 T_1}{\partial z^2} + \dot{Q} - G \cdot (T_1 - T_2), \tag{4a}$$

$$\frac{\partial C_2 T_2}{\partial t} = G \cdot (T_1 - T_2). \tag{4b}$$

Here T_1 and T_2 are the temperatures of cross-plane and in-plane phonons; G is the in-plane and cross-plane phonon energy coupling coefficient. The energy exchange among C_1 and C_2 is very fast, so most of the time C_1 and C_2 are in equilibrium. But in fact they are involved in heat conduction in two different directions.

The volumetric heat capacity can be calculated by using the following equation:

$$C = \sum_j \int_0^{\omega_D} g(\omega) k_B \left(\frac{\hbar\omega}{k_B T}\right)^2 \frac{e^{\hbar\omega/k_B T}}{\left(e^{\hbar\omega/k_B T} - 1\right)^2} d\omega \tag{5}$$

among which, ω_D is the upper cut-off frequency for each phonon branch, $\hbar$ the Planck's constant; $g(\omega)$ the density of state of the phonon branches. Fig. 7b shows the reproduced density of state of phonon branches in graphite from Nichlow's work [71]. As described before, the upper cut-off frequencies for the phonon branches are no higher than 4 THz along the c-axis. Here, we take ω_D = 4 THz and calculate the heat capacity from contribution of low-frequency phonons along with temperature from 12.3 K to 295 K. However, this calculated heat capacity (C) does not involve in c-axis heat conduction all the way as it has an acoustic phonon branch that contributes almost equally in three directions. As shown in Fig. 7a, the LA branch in the (001) direction corresponds to the ZA branch in the (100) direction in terms of lattice vibration direction. The wavevectors of this phonon branch have comparable components in the (100) and (001) directions under 4 THz. This means this phonon branch contributes equally in the 3D structure and lead to a factor of $1/3 \times 1/3 = 1/9$ in the heat capacity for cross-plane heat conduction. The two TA phonon branches in the (001) direction correspond to the LA and TA branches in the (100) direction in terms of lattice vibration direction. The wavevectors of these two branches have negligible components in the (100) direction under 4 THz, meaning the phonons will mainly propagate in the c-axis direction. This leads to a factor of 2/3 in the heat capacity for cross-plane heat conduction. Thus, we have a factor of 7/9 in the heat capacity that contributes to the thermal transport in the cross-plane direction which can be expressed as $C_1 = 7/9\ C$. In this case, a modified 1D kinetic theory ($k_c = C_1 v l$) is used for the c-axis thermal conductivity of GP.

The calculation results of the specific heat are shown in Fig. 7c, from which we can see the c-axis specific heat (c_1, corresponding to C_1) increases from 1.42 $Jkg^{-1}K^{-1}$ at 12.3 K and reach the maximum value of 35.7 $Jkg^{-1}K^{-1}$ at near 180 K (corresponding to the cut-off frequency of 4 THz) and then stay almost constant as temperature increases. For comparison, the total specific heat (c_p: black rectangles) are also calculated by using Eq. (5) with the upper cut-off frequency of about 48 THz from the in-plane LA phonon branches, which corresponds to a Debye temperature of about 2300 K [77]. The calculated total specific heat increases from 1.83 $Jkg^{-1}K^{-1}$ at 12.3 K to 601 $Jkg^{-1}K^{-1}$ at 295 K and will keep increasing until the temperature reaches the Debye temperature [78]. This calculated total specific heat is close to the well-accepted specific heat of graphite [54], which in other words proves the accuracy of the calculation. The discrepancies come from the ignorance of contribution from optical phonon branches and the errors during reproducing the density of state of phonons (Fig. 7b).

According to the recent MD simulations of Wei et al. [29], the defect-free k_c of bulk graphite is 11.6 $Wm^{-1}K^{-1}$ at 300 K. With the calculated specific heat and average phonon group velocity, the c-MFP is calculated as 165 nm at RT based on our modified 1D kinetic theory described before. The calculated c-MFP is a little larger than 146 nm determined by Wei et al. [29] in the MD simulations, but still proves the accuracy of our treatment of the phonon modes contribution to thermal transport along the c-axis. With the fitted k_c from the PLTR2 measurements, the thermal diffusivity of GP in the cross-plane direction is calculated by $\alpha_c = k_c/C_1$. The red circles in Fig. 7d shows the calculation results based on the c-axis heat capacity (C_1) while the black rectangles (macroscale thermal diffusivity) show those with the total heat capacity. Also shown in Fig. 7d are the in-plane thermal diffusivities of GP from our recent work [41]. The thermal diffusivities calculated by using C_1 is much larger than those calculation with the total heat capacity, indicating the thermal transport response rate is larger than we used to think. Another interesting observation in Fig. 7d is that the red curve is parallel to the blue and olive ones at not-too-low temperatures, meaning thermal diffusivities of GP in the in-plane direction have a relatively constant ratio (about 30) to those in the cross-plane direction against temperature. This anisotropy of thermal diffusivity is one order of magnitude smaller than that of thermal conductivity

(around 300).

4.2. Defect level and phonon mean free path uncovered by the thermal reffusivity theory

The thermal conductivity defines how well a material conducts heat while the thermal diffusivity defines how fast the material responds to thermal impulse. Here we use another parameter, the thermal reffusivity, reciprocal of the thermal diffusivity, to study the phonons contribution to thermal transport in GP along the *c*-axis. The thermal reffusivity was first defined by Xu et al. in our lab to characterize the phonon thermal resistivity of DNA [79] and has been successfully used in investigating the defect level and structure domain size in other materials including graphene foam [80] and ultrahigh molecular weight polyethylene (UHMWPE) [81]. Like thermal diffusivity, thermal reffusivity eliminates the temperature-dependent heat capacity involved in thermal conductivity and is solely determined by the phonon propagation and scattering in the material. With the modified kinetic theory described before, thermal reffusivity of cross-plane phonons is simply expressed as the following equation:

$$\Theta = \frac{C_1}{k_c} = \frac{1}{vl}. \tag{6}$$

Combing with Eq. (3), we have $\Theta = v^{-1}(l_U^{-1} + l_{boundary}^{-1} + l_{defects}^{-1}) = \Theta_0 + \Theta_i$ where Θ_0 is the boundary and defect scattering induced thermal reffusivity and Θ_i is the U-scattering induced thermal reffusivity. As described before, when temperature goes down and approaches 0 K, U-scattering vanishes and Θ_i goes to zero. Therefore, the residual thermal reffusivity (Θ_0) at the 0 K limit can help reveal the structural domain size and defect level of the material.

The role of Θ in thermal transport is similar to that of electric resistivity (ρ) in metals (like the Ir coating in this work). If there is no defect, Θ and ρ should approach zero as temperature goes down to 0 K. If the defects in the materials have scattering effect, when temperature goes to 0 K, Θ and ρ will have finite residual values. The black circles in Fig. 8a show the calculated Θ of GP in the cross-plane direction against temperature. We can see Θ decreases as temperature goes down and reaches almost a specific value at lower temperatures, just as predicted by the thermal reffusivity theory. The rising values at very low temperatures are mainly due to the nonlinear relationship between ρ of the Ir coating and the temperature at very low temperatures. The nonlinearity is induced by the very low phonon population and its strong nonlinear correlation with temperature in Ir coating. This dominates the electron scattering behavior at low temperatures and how ρ varies with temperature. In this case, the temperature coefficient of ρ of Ir coating at temperatures lower than 50 K is much smaller than that at higher temperatures. Especially at temperatures lower than 30 K, this coefficient is much smaller than that at high temperatures. This means the real temperature rising is indeed much faster than the voltage or electrical resistance rising observed in the experiment. In this case, k_c of GP is underestimated in the fitting process, which will finally lead to the overestimation of thermal reffusivity. Note that, this overestimation is getting more remarkable at extremely low temperatures due to the continuing decrease of the temperature coefficient of ρ as temperature decreases. In addition, at very low temperatures, the ratio of Θ of GP in the total Θ of the GP/PMMA/PET multilayered films will get much smaller where small differences in the experimental data or the known parameters would lead to much larger deviations in the fitting results. Our numerical calculations show that the fitting curves in this temperature range are not sensitive to the trial values of k_c and the uncertainties of k_c in this range may be as large as 50%.

From the exponential fitting (red curve in Fig. 8a), Θ_0 of GP is determined at 4809 sm^{-2}, taking 37% of Θ at RT. Using Eq. (6), with $v = 890$ m/s, *c*-MFP is calculated as 234 nm at the 0 K limit, which is only induced by the defect and boundary scattering and should be smaller than the crystallite sizes of GP in the cross-plane direction. The blue triangles and the green curve in Fig. 8a show the thermal reffusivity and corresponding exponential fitting of the well-annealed pyrolytic graphite from literature [58]. Here, Θ_0 of this graphite is determined at 2994 sm^{-2}, taking only 22% of Θ at RT. This proves the better structure and low defect level in the graphite than in our GP sample. Accordingly, *c*-MFP is calculated as 375 nm at the 0 K limit, which is close to the 404 nm grain size calculated from the TEM images in the most recent experimental work by Zhang et al. [31], and is also consistent with the estimated *c*-MFP spectrum (100–600 nm) at very low temperature in the same work. The magenta and olive rectangles in Fig. 8a shows the experimental results of the in-plane thermal reffusivity of GP measured in our recent work for comparison purpose. The in-plane MFP limited by defects and boundaries or the crystallite size is estimated as 1.68 μm [41]. The estimated *c*-MFP or cross-plane crystallite size is less than one order of magnitude smaller than that in the in-plane direction, which is seemingly inconsistent with the large anisotropy in thermal conductivity of graphite (around 300). This comparison, however, indicates that the large anisotropy is not mainly due to the strong scattering mechanisms induced by small cross-plane crystallite size. Based on Eq. (6), the sample *c*-

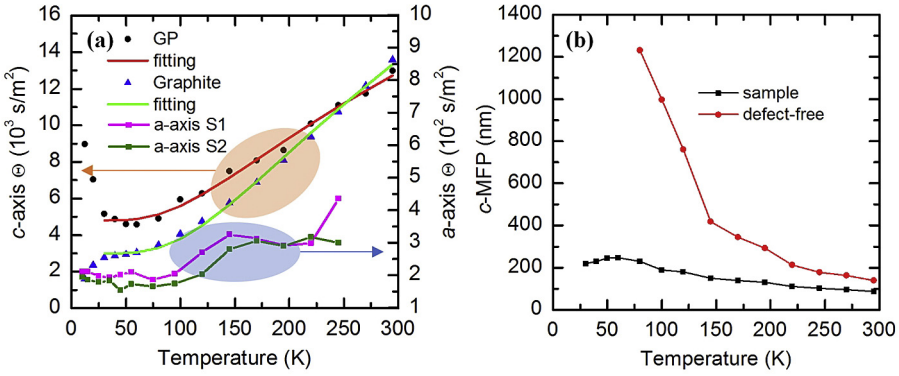

Fig. 8. Thermal reffusivity and *c*-MFP. (a) *c*-axis thermal reffusivity of GP and graphite calculated in this work and *a*-axis thermal reffusivity of GP calculated in our previous work [41]. Also shown are the exponential fitting curves to the *c*-axis thermal reffusivity that are used to extract the residual thermal reffusivity. (b) Sample and defect-free *c*-MFPs of GP. (A colour version of this figure can be viewed online.)

MFP of GP is calculated against temperature. Also by subtracting Θ_0 from Θ, Θ_i is obtained, from which the defect-free k_c and c-MFP of GP are calculated. The defect-free k_c of GP is calculated at 9.67 $Wm^{-1}K^{-1}$ at RT, close to 11.6 $Wm^{-1}K^{-1}$ of graphite from the previous MD simulations [29]. Fig. 8b shows the sample c-MFP and the extracted defect-free c-MFP of GP. The defect-free c-MFP is 138 nm at RT and would increases to infinite values as temperature decreases and approaches 0 K. This is because we eliminate the extrinsic scattering from defects and boundaries and the U-scattering will also vanish at extremely low temperatures. The sample c-MFP also increases as temperature decreases but reach a relatively constant value at extremely low temperatures due to the defect and boundary scattering.

The determined sample and defect-free c-MFPs of GP (86.7 and 138 nm, respectively) at RT are orders of magnitude larger than those derived from the classic kinetic theory [25]. The problem with the classic kinetic theory is that the expression is based on the isotropic model and assume that the heat capacity is contributed equally by phonon modes over the entire Brillouin zone. While in fact only low-frequency phonons under 4 THz are supported in the cross-plane direction and contribute to the heat capacity and thermal transport in that direction [82]. Our modification of the kinetic theory takes into account the high anisotropy of phonon dispersions and calculates only the contributions of cross-plane phonon modes to the heat capacity. This simple treatment can help explain the long phonon propagating distances yet small thermal conductivity of GP along the c-axis. Our extracted defect-free c-MFP at RT (138 nm) is consistent with the long c-MFP of graphite, which is estimated as 146 nm in the recent MD simulations by Wei et al. [29] Following experimental work by Fu et al. [30] even reported a longer average c-MFP (204 nm) at RT by employing the 3ω measurement on graphite films of varying thicknesses. Most recent experimental work by Zhang et al. [31] performed the TDTR measurement on graphite films and reported a c-MFP in the range of 100–200 nm at RT. The extracted c-MFP at 0 K limit (234 nm) also serves as a good estimation of the crystallite size of GP along the c-axis. As mentioned in the sample characterization section, the crystallite size cannot be directly determined from the XRD measurement. This, in other words, proves that the crystallite size is in the order of several hundred nanometers which is beyond the instrument measurement range. Note the Raman spectra show that the graphene flakes contain 5–6 layers graphene, corresponding to a thickness of 1.68–2.01 nm. The determined c-axis structure size (234 nm) is much larger than the flake thickness, uncovering the excellent c-axis atomic structure order. Also this c-axis structure size is much larger than the defect-free c-MFP (138 nm) at RT. Therefore the effective c-MFP at RT is not significantly reduced, but stays at a quite high level of 86.7 nm.

5. Conclusion

By employing the PLTR2 technique, the thermal transport properties of GP in the cross-plane direction (c-axis) were investigated within a temperature range from 295 K to 12.3 K. The determined k_c is 6.08 ± 0.6 $Wm^{-1}K^{-1}$ at RT, close to the values (5.7–6.8 $Wm^{-1}K^{-1}$) of graphite along the c-axis. The measurement accuracy was also verified by the PT technique on the same GP, which gave a value of 5.38 ± 0.54 $Wm^{-1}K^{-1}$ at RT. Taking into account the large anisotropy of phonon dispersions, we developed a model and identified the phonons and their specific heat that sustain the heat conduction in the c-axis. The validity of our model was verified by predicting the c-MFP of graphite. Our model predicted a c-MFP of 165 nm for ideal graphite at RT, very close to the value of 146 nm by MD modeling. For widely studied graphite samples, our model predicted a structure domain size of 375 nm, close to the 404 nm grain size calculated from the TEM images. By studying the thermal reffusivity variation against temperature, we suppressed the measurement uncertainties and calculated the c-MFP induced by the defect and boundary scattering at 0 K limit. This determined c-MFP is about 234 nm, a good estimation of the structural domain size and defect levels in our GP sample as the Umklapp phonon-phonon scattering vanishes at the 0 K limit. This structure domain size is much smaller than the in-plane one (1.68 μm), but still significantly exceeds the graphene flake thickness (1.68–2.01 nm) in our GP, uncovering quite long-range structural order among graphene flakes. By subtracting the effect of these extrinsic scattering from defects and grain boundaries, we calculated the defect-free k_c and c-MFP of GP with the modified kinetic theory. At RT, the defect-free k_c is 9.67 $Wm^{-1}K^{-1}$, close to 11.6 $Wm^{-1}K^{-1}$ of graphite from the recent MD simulations. The defect-free c-MFP is 138 nm at RT, just a little smaller than 146 nm (graphite) from MD simulations, which is consistent with the recent accepted theory of long c-MFP. This work along with our recent work in the in-plane direction thermal transport of GP, give a full picture of the thermal transport properties of GP which is of great importance in its industrial applications.

Acknowledgement

Support of this work by National Science Foundation (CBET1235852, CMMI1264399), Department of Energy (DENE0000671, DEEE0007686), and Iowa Energy Center (MG-16-025, OG-17-005) is gratefully acknowledged.

References

[1] K.S. Novoselov, A.K. Geim, S.V. Morozov, D. Jiang, Y. Zhang, S.V. Dubonos, et al., Electric field effect in atomically thin carbon films, Science 306 (5696) (2004) 666–669.
[2] M.A. Worsley, P.J. Pauzauskie, T.Y. Olson, J. Biener, J.H. Satcher Jr., T.F. Baumann, Synthesis of graphene aerogel with high electrical conductivity, J. Am. Chem. Soc. 132 (40) (2010) 14067–14069.
[3] A.A. Balandin, S. Ghosh, W.Z. Bao, I. Calizo, D. Teweldebrhan, F. Miao, et al., Superior thermal conductivity of single-layer graphene, Nano Lett. 8 (3) (2008) 902–907.
[4] C. Wang, L. Zhang, Z. Guo, J. Xu, H. Wang, K. Zhai, et al., A novel hydrazine electrochemical sensor based on the high specific surface area graphene, Microchim. Acta 169 (1–2) (2010) 1–6.
[5] H. Sun, Z. Xu, C. Gao, Multifunctional, ultra-flyweight, synergistically assembled carbon aerogels, Adv. Mater 25 (18) (2013) 2554–2560.
[6] F. Xia, T. Mueller, Y.-M. Lin, A. Valdes-Garcia, P. Avouris, Ultrafast graphene photodetector, Nat. Nanotechnol. 4 (12) (2009) 839–843.
[7] X. Wang, L. Zhi, K. Müllen, Transparent, conductive graphene electrodes for dye-sensitized solar cells, Nano Lett. 8 (1) (2008) 323–327.
[8] F. Bonaccorso, Z. Sun, T. Hasan, A. Ferrari, Graphene photonics and optoelectronics, Nat. Phot. 4 (9) (2010) 611–622.
[9] D. Cohen-Tanugi, J.C. Grossman, Water desalination across nanoporous graphene, Nano Lett. 12 (7) (2012) 3602–3608.
[10] A. Gugliuzza, A. Politano, E. Drioli, The advent of graphene and other two-dimensional materials in membrane science and technology, Curr. Opin. Chem. Eng. 16 (2017) 78–85.
[11] K.M. Shahil, A.A. Balandin, Thermal properties of graphene and multilayer graphene: applications in thermal interface materials, Solid State Commun. 152 (15) (2012) 1331–1340.
[12] S. Ghosh, I. Calizo, D. Teweldebrhan, E.P. Pokatilov, D.L. Nika, A.A. Balandin, et al., Extremely high thermal conductivity of graphene: prospects for thermal management applications in nanoelectronic circuits, Appl. Phys. Lett. 92 (15) (2008), 151911.
[13] S. Ghosh, D. Nika, E. Pokatilov, A. Balandin, Heat conduction in graphene: experimental study and theoretical interpretation, NJPh 11 (9) (2009), 095012.
[14] S. Ghosh, W. Bao, D.L. Nika, S. Subrina, E.P. Pokatilov, C.N. Lau, et al., Dimensional crossover of thermal transport in few-layer graphene, Nat. Mater 9 (7) (2010) 555–558.
[15] P. Klemens, D. Pedraza, Thermal conductivity of graphite in the basal plane, Carbon 32 (4) (1994) 735–741.
[16] C. Faugeras, B. Faugeras, M. Orlita, M. Potemski, R.R. Nair, A. Geim, Thermal conductivity of graphene in corbino membrane geometry, ACS Nano 4 (4) (2010) 1889–1892.
[17] J.-U. Lee, D. Yoon, H. Kim, S.W. Lee, H. Cheong, Thermal conductivity of

suspended pristine graphene measured by Raman spectroscopy, PhRvB 83 (8) (2011), 081419.
[18] S. Chen, Q. Wu, C. Mishra, J. Kang, H. Zhang, K. Cho, et al., Thermal conductivity of isotopically modified graphene, Nat. Mater 11 (3) (2012) 203–207.
[19] A.J. Schmidt, K.C. Collins, A.J. Minnich, G. Chen, Thermal conductance and phonon transmissivity of metal–graphite interfaces, J. Appl. Phys. 107 (10) (2010), 104907.
[20] Y.K. Koh, M.-H. Bae, D.G. Cahill, E. Pop, Heat conduction across monolayer and few-layer graphenes, Nano Lett. 10 (11) (2010) 4363–4368.
[21] Z. Chen, W. Jang, W. Bao, C. Lau, C. Dames, Thermal contact resistance between graphene and silicon dioxide, Appl. Phys. Lett. 95 (16) (2009), 161910.
[22] G.A. Slack, Anisotropic thermal conductivity of pyrolytic graphite, PhRv 127 (3) (1962) 694.
[23] R. Taylor, The thermal conductivity of pyrolytic graphite, PMag 13 (121) (1966) 157–166.
[24] F.P. Incropera, A.S. Lavine, T.L. Bergman, D.P. DeWitt, Fundamentals of Heat and Mass Transfer, Wiley, 2007.
[25] T. Tanaka, H. Suzuki, The thermal diffusivity of pyrolytic graphite at high temperatures, Carbon 10 (3) (1972) 253–257.
[26] Z. Wei, Z. Ni, K. Bi, M. Chen, Y. Chen, Interfacial thermal resistance in multilayer graphene structures, Phys. Lett. A 375 (8) (2011) 1195–1199.
[27] M. Harb, C. von Korff Schmising, H. Enquist, A. Jurgilaitis, I. Maximov, P. Shvets, et al., The c-axis thermal conductivity of graphite film of nanometer thickness measured by time resolved X-ray diffraction, Appl. Phys. Lett. 101 (23) (2012), 233108.
[28] M.M. Sadeghi, I. Jo, L. Shi, Phonon-interface scattering in multilayer graphene on an amorphous support, Proc. Natl. Acad. Sci. 110 (41) (2013) 16321–16326.
[29] Z. Wei, J. Yang, W. Chen, K. Bi, D. Li, Y. Chen, Phonon mean free path of graphite along the c-axis, Appl. Phys. Lett. 104 (8) (2014), 081903.
[30] Q. Fu, J. Yang, Y. Chen, D. Li, D. Xu, Experimental evidence of very long intrinsic phonon mean free path along the c-axis of graphite, Appl. Phys. Lett. 106 (3) (2015), 031905.
[31] H. Zhang, X. Chen, Y.-D. Jho, A.J. Minnich, Temperature-dependent mean free path spectra of thermal phonons along the c-Axis of graphite, Nano Lett. 16 (3) (2016) 1643–1649.
[32] F. Liu, S. Song, D. Xue, H. Zhang, Folded structured graphene paper for high performance electrode materials, Adv. Mater 24 (8) (2012) 1089–1094.
[33] H. Wu, L.T. Drzal, Graphene nanoplatelet paper as a light-weight composite with excellent electrical and thermal conductivity and good gas barrier properties, Carbon 50 (3) (2012) 1135–1145.
[34] J.K. Lee, K.B. Smith, C.M. Hayner, H.H. Kung, Silicon nanoparticles–graphene paper composites for Li ion battery anodes, Chem. Commun. 46 (12) (2010) 2025–2027.
[35] H. Gwon, H.-S. Kim, K.U. Lee, D.-H. Seo, Y.C. Park, Y.-S. Lee, et al., Flexible energy storage devices based on graphene paper, Energy & Environ. Sci. 4 (4) (2011) 1277–1283.
[36] N.-J. Song, C.-M. Chen, C. Lu, Z. Liu, Q.-Q. Kong, R. Cai, Thermally reduced graphene oxide films as flexible lateral heat spreaders, J. Mater. Chem. A 2 (39) (2014) 16563–16568.
[37] G. Xin, H. Sun, T. Hu, H.R. Fard, X. Sun, N. Koratkar, et al., Large-area freestanding graphene paper for superior thermal management, Adv. Mater. 26 (26) (2014) 4521–4526.
[38] O.C. Compton, D.A. Dikin, K.W. Putz, L.C. Brinson, S.T. Nguyen, Electrically conductive "alkylated" graphene paper via chemical reduction of amine-functionalized graphene oxide paper, Adv. Mater. 22 (8) (2010) 892–896.
[39] J. Xiang, L.T. Drzal, Thermal conductivity of exfoliated graphite nanoplatelet paper, Carbon 49 (3) (2011) 773–778.
[40] C. Vallés, J.D. Núñez, A.M. Benito, W.K. Maser, Flexible conductive graphene paper obtained by direct and gentle annealing of graphene oxide paper, Carbon 50 (3) (2012) 835–844.
[41] Y. Xie, P. Yuan, T. Wang, N. Hashemi, X. Wang, Switch on the high thermal conductivity of graphene paper, Nanoscale 8 (40) (2016) 17581–17597.
[42] X. Feng, G. Liu, S. Xu, H. Lin, X. Wang, 3-dimensional anisotropic thermal transport in microscale poly (3-hexylthiophene) thin films, Poly 54 (7) (2013) 1887–1895.
[43] W. Parker, R. Jenkins, C. Butler, G. Abbott, Flash method of determining thermal diffusivity, heat capacity, and thermal conductivity, J. Appl. Phys. 32 (9) (1961) 1679–1684.
[44] S. Min, J. Blumm, A. Lindemann, A new laser flash system for measurement of the thermophysical properties, Thermochim. Acta 455 (1) (2007) 46–49.
[45] W. Hohenauer, L. Vozár, An Estimation of thermophysical properties of layered materials by the laser-flash method, High. Temp. - High. Press. 33 (1) (2001) 17–26.
[46] J. Guo, X. Wang, D.B. Geohegan, G. Eres, C. Vincent, Development of pulsed laser-assisted thermal relaxation technique for thermal characterization of microscale wires, J. Appl. Phys. 103 (11) (2008), 113505.
[47] W. Yu, G. Liu, J. Wang, X. Huang, H. Xie, X. Wang, Significantly reduced anisotropic phonon thermal transport in graphene oxide films, Synth. React. Inorg. M. 43 (9) (2013) 1197–1205.
[48] T.A. Pham, J.S. Kim, J.S. Kim, Y.T. Jeong, One-step reduction of graphene oxide with L-glutathione, Colloid Surf. A physicochem. Eng. Asp. 384 (1) (2011) 543–548.
[49] D. Graf, F. Molitor, K. Ensslin, C. Stampfer, A. Jungen, C. Hierold, et al., Spatially resolved raman spectroscopy of single- and few-layer graphene, Nano Lett. 7 (2) (2007) 238–242.
[50] X. Wang, Y.P. Chen, D.D. Nolte, Strong anomalous optical dispersion of graphene: complex refractive index measured by Picometrology, Opt. Express 16 (26) (2008) 22105–22112.
[51] T. Lee, Thermal Diffusivity of Dispersed and Layered Composites Purdue University, Lafayette, 1977.
[52] T.P. Melia, Thermodynamic functions of linear high polymers .8. Methylmethacrylate and polymethylmethacrylate, Poly 3 (3) (1962) 317–318.
[53] T. Barron, G.K. White, Heat Capacity and Thermal Expansion at Low Temperatures, Springer Science & Business Media, 2012.
[54] W. DeSorbo, W. Tyler, The specific heat of graphite from 13 to 300 K, J. Chem. Phys. 21 (10) (1953) 1660–1663.
[55] R.O. Pohl, X. Liu, E. Thompson, Low-temperature thermal conductivity and acoustic attenuation in amorphous solids, RvMP 74 (4) (2002) 991–1013.
[56] C. Choy, D. Greig, The low temperature thermal conductivity of isotropic and oriented polymers, J. Phys. C Solid State Phys. 10 (2) (1977) 169.
[57] C.L. Choy, Thermal-conductivity of polymers, Poly 18 (10) (1977) 984–1004.
[58] C.Y. Ho, R.W. Powell, P.E. Liley, Thermal conductivity of the Elements: a Comprehensive Review, DTIC Document, 1974.
[59] M. Shen, P.K. Schelling, P. Keblinski, Heat transfer mechanism across few-layer graphene by molecular dynamics, PhRvB 88 (4) (2013), 045444.
[60] W. Jang, Z. Chen, W. Bao, C.N. Lau, C. Dames, Thickness-dependent thermal conductivity of encased graphene and ultrathin graphite, Nano Lett. 10 (10) (2010) 3909–3913.
[61] X. Chen, Y. He, Y. Zhao, X. Wang, Thermophysical properties of hydrogenated vanadium-doped magnesium porousnanostructures, Nanot 21 (5) (2009), 055707.
[62] T. Wang, X.W. Wang, Y.W. Zhang, L.Y. Liu, L. Xu, Y. Liu, et al., Effect of zirconium(IV) propoxide concentration on the thermophysical properties of hybrid organic-inorganic films, J. Appl. Phys. 104 (1) (2008), 013528.
[63] H.P. Hu, X.W. Wang, X.F. Xu, Generalized theory of the photoacoustic effect in a multilayer material, J. Appl. Phys. 86 (7) (1999) 3953–3958.
[64] A. Al Taleb, D. Farías, Phonon dynamics of graphene on metals, J. Phys. Condens. Matter 28 (10) (2016), 103005.
[65] A. Politano, Spectroscopic investigations of phonons in epitaxial graphene, Crit. Rev. Solid State Mater. Sci. 42 (2) (2017) 99–128.
[66] J.-A. Yan, W. Ruan, M. Chou, Phonon dispersions and vibrational properties of monolayer, bilayer, and trilayer graphene: density-functional perturbation theory, PhRvB 77 (12) (2008), 125401.
[67] C.T. Nai, H. Xu, S.J. Tan, K.P. Loh, Analyzing dirac cone and phonon dispersion in highly oriented nanocrystalline graphene, ACS nano 10 (1) (2015) 1681–1689.
[68] A. Politano, A.R. Marino, G. Chiarello, Phonon dispersion of quasi-freestanding graphene on Pt (111), J. Phys. Condens. Matter 24 (10) (2012), 104025.
[69] A. Politano, A.R. Marino, D. Campi, D. Farías, R. Miranda, G. Chiarello, Elastic properties of a macroscopic graphene sample from phonon dispersion measurements, Carbon 50 (13) (2012) 4903–4910.
[70] A. Allard, L. Wirtz, Graphene on metallic substrates: suppression of the Kohn anomalies in the phonon dispersion, Nano Lett. 10 (11) (2010) 4335–4340.
[71] R. Nicklow, N. Wakabayashi, H. Smith, Lattice dynamics of pyrolytic graphite, PhRvB 5 (12) (1972) 4951.
[72] P. Anees, M. Valsakumar, S. Chandra, B. Panigrahi, Ab initio study on stacking sequences, free energy, dynamical stability and potential energy surfaces of graphite structures, Modell. Simul. Mater. Sci. Eng. 22 (3) (2014), 035016.
[73] N. Mounet, N. Marzari, First-principles determination of the structural, vibrational and thermodynamic properties of diamond, graphite, and derivatives, PhRvB 71 (20) (2005), 205214.
[74] L. Wirtz, A. Rubio, The phonon dispersion of graphite revisited, Solid State Commun. 131 (3) (2004) 141–152.
[75] D.L. Nika, A.A. Balandin, Two-dimensional phonon transport in graphene, J. Phys. Condens. Matter 24 (23) (2012), 233203.
[76] M. Holland, Analysis of lattice thermal conductivity, PhRv 132 (6) (1963) 2461.
[77] V.K. Tewary, B. Yang, Singular behavior of the Debye-Waller factor of graphene, PhRvB 79 (12) (2009), 125416.
[78] A. Politano, B. Borca, M. Minniti, J. Hinarejos, A.V. de Parga, D. Farías, et al., Helium reflectivity and Debye temperature of graphene grown epitaxially on Ru (0001), PhRvB 84 (3) (2011), 035450.
[79] Z. Xu, X. Wang, H. Xie, Promoted electron transport and sustained phonon transport by DNA down to 10 K, Poly 55 (24) (2014) 6373–6380.
[80] Y. Xie, Z. Xu, S. Xu, Z. Cheng, N. Hashemi, C. Deng, et al., The defect level and ideal thermal conductivity of graphene uncovered by residual thermal reffusivity at the 0 K limit, Nanoscale 7 (22) (2015) 10101–10110.
[81] J. Liu, Z. Xu, Z. Cheng, S. Xu, X. Wang, Thermal conductivity of ultrahigh molecular weight polyethylene crystal: defect effect uncovered by 0 K limit phonon diffusion, ACS Appl. Mater. Interfaces 7 (49) (2015) 27279–27288.
[82] A. Minnich, Exploring the extremes of heat conduction in anisotropic materials, Nanosci. Microsci. Therm. 20 (1) (2016) 1–21.